Enhancing surface charge density of Graphene Oxide membranes through Al(OH)4 anion incorporation for osmotic energy conversion

ADVANCED ENERGY & SUSTAINABILITY RESEARCH
Open Access
www.advenergysustres.com

Enhancing Surface Charge Density of Graphene Oxide Membranes through $Al(OH)_4^-$ Anion Incorporation for Osmotic Energy Conversion

Anna Aixalà-Perelló, Federico Raffone, Luisa Baudino, Alessandro Pedico, Mara Serrapede, Giancarlo Cicero, and Andrea Lamberti*

Graphene oxide (GO) has been extensively studied for fabricating ion exchange membranes. This material is of interest due to its surface-governed charge which, combined with the interlayer distance between the GO flakes stack, offers ion selectivity. However, obtaining high-performing membranes with high ion selectivity and low ionic resistance remains challenging. To address this issue, $Al(OH)_4^-$ anions are incorporated into graphene oxide membranes to increase their spontaneous negative surface charge. The anions are successfully formed and encapsulated through a reaction with the alumina support under alkaline conditions during the membrane fabrication. A modeling of the system proves the anchoring of the $Al(OH)_4^-$ anions within the GO matrix. The incorporation of these anions significantly improves the permselectivity and reduces the ionic resistance, reaching approximately 95% and 2 $\Omega\,cm^2$, respectively. The GO-modified membranes also present mono-valent selectivity, which can boost reverse electrodialysis power densities.

1. Introduction

Energy is one of the main factors affecting climate change, accounting for around 60% of all global greenhouse gas emissions.[1,2] Therefore, a major push for developing renewable energies is necessary to reduce their impact.

Blue energy (also called salinity gradient power - SGP) has arisen as a renewable energy that guarantees continuous energy generation compared to other renewable energies (i.e., solar and wind) which present intermittent production. This technology is based on the energy captured from the increase in entropy when mixing water with different salinities.[3] Theoretical calculations indicate that a stream flowing at 1 $m^3\,s^{-1}$ could produce 1 MW of electricity,[3] and that specific energy levels ranging from 0.44 to 0.76 kWh m^{-3} can be obtained by mixing river water and seawater, with the exact value dependent on the salinity ratio.[4–6] Academic research estimates the global potential power output to be approximately 2TW when using the global discharge of rivers into the seas, representing nearly 80% of the total global energy demand.[3,7,8]

Some technologies proposed to harvest this energy are pressure retarded osmosis, reverse electrodialysis (RED), and capacitive mixing.[9]

RED uses ion exchange membranes, which are charged permselective membranes. Cation exchange membranes (CEM) are negatively charged membranes that allow the passage of cations, whereas anion exchange membranes are positively charged membranes that are selective to anions. In a RED system, a stack of alternating cation and anion exchange membranes is used with high and low-concentrated solutions on either side of each membrane. The combination of the charge of the membranes and the salinity gradient forces the flow of cations and anions in opposite directions, developing an electrical potential at the membrane. Afterwards, the ionic current generated is converted into electricity by redox reactions at the electrodes connected to an external circuit.[10,11]

Membrane performance is a key issue for the success of this technology, with efficiency and durability being the most important features. The most important properties of ion exchange membranes (IEMs) are high selectivity, low ionic resistance, high mechanical and chemical stability, and low cost. In contrast, the fabrication processes of IEMs are not energy efficient and often use toxic reagents.[11] 2D materials have been proposed to increase the power density given their surface-governed ion transport dynamics.[12–17] In fact, their selectivity comes from the electrostatic interaction of the ions with the charged surface of the material. MXenes, black phosphorous (BP), and graphene oxide (GO) are examples of nanolaminated membranes made

A. Aixalà-Perelló, F. Raffone, L. Baudino, A. Pedico, M. Serrapede, G. Cicero, A. Lamberti
Politecnico di Torino
Dipartimento di Scienza Applicata e Tecnologia (DISAT)
Corso Duca Degli Abruzzi, 24, 10129 Torino, Italy
E-mail: anna.aixala@polito.it

A. Aixalà-Perelló, A. Pedico, M. Serrapede, A. Lamberti
Istituto Italiano di Tecnologia
Center for Sustainable Future Technologies
Via Livorno 60, 10144 Torino, Italy

The ORCID identification number(s) for the author(s) of this article can be found under https://doi.org/10.1002/aesr.202400090.

DOI: 10.1002/aesr.202400090

from 2D nanomaterials.[13,18–23] Studies in the literature have shown that the power density of nanofluidic membranes for osmotic power energy harvesting is reduced when the size of the testing membrane increases (see Figure S1, Supporting Information). This can be attributed to multiple factors when scaling up a system, for example, the increase of the reservoir resistance, reservoir/nanopores interfacial resistance, and the increased amount of stochastic physical defects within the membrane.[20,24–27] Despite this trend, this work presents the use of GO membranes at a significantly larger scale with performances comparable to the ones of commercially available ion exchange membranes for this kind of application.

GO membranes are composed of a series of stacked flakes, forming lamellar nanostructures with 2D planar nanochannels.[28,29] The structural integrity of these stacks relies on the presence of π–π bonds in the sp^2 regions of GO and hydrogen bonds between the oxidized moieties in the sp^3 regions.[29] These nanochannels exhibit remarkable characteristics, facilitating both ultrafast ion transport and ion sieving, thanks to the interlayer distance between the flakes (d-spacing), which imposes a cut-off rejection for ions with a hydrated radius above 4.5 Å.[30] Moreover, the presence of oxygenated functional groups not only enables the formation of the membrane stack but also provides a negative charge, responsible for the charge selectivity of the membrane, or the so-called Donnan exclusion.

Different strategies have been proposed to enhance ion rejection while controlling the d-spacing of the GO membrane: partial reduction,[22,31,32] physical confinement,[19] chemical crosslinking,[18,33] intercalating agents,[34–37] and surface modification.[38] Nevertheless, membrane modification and the incorporation of intercalating agents can cause blockage, enlargement, or destruction of the uniformity of the nanochannels, leading to a negative impact on the final power density.[37]

Herein, we propose an innovative approach to enhance the permselectivity and reduce the ionic resistance of the GO matrix by incorporating $Al(OH)_4^-$ ions. This incorporation results in an augmented surface negative charge, further enhancing the performance of the membrane. In this study, we present a simple and efficient method for introducing these ions into the nanochannels through a reaction between the alumina support used for the membrane fabrication and a basic graphene oxide dispersion. A supporting model confirmed the anchoring of these ions, which enhanced the cation transport and limited the anion diffusion, thus improving the power output.

2. Results and Discussion

GO membranes were prepared by vacuum filtration and $Al(OH)_4^-$ ions were successfully inserted in their structure (denoted as GO-KOH membranes from now on). This was achieved thanks to the reaction of the alumina support used for the membrane fabrication with the alkaline GO dispersion. Previous studies have demonstrated the impact of pH on the corrosion of alumina supports,[39] reporting the release of Al^{3+} ions from the support during the filtration of an acid. They demonstrated the crosslinking of the Al^{3+} cations with the membrane sheets, thereby reinforcing the membrane structure. However, in this work, it was observed that in alkaline media the support reacts to form $KAl(OH)_4$ in aqueous conditions (as indicated by Equation (1)). During the fabrication process and the reaction with the support, isolated $Al(OH)_4^-$ anions remain trapped within GO layers as negative ions with counter ions (K^+) nearby.

$$Al_2O_3 + 2\,KOH + 3\,H_2O \rightarrow 2\,KAl(OH)_4 \quad (1)$$

2.1. Membrane Characterization

Homogeneous and highly aligned membrane layers with a thickness of 26 ± 2 µm were successfully obtained by vacuum filtration (see **Figure 1**a–c). Analyses using energy-dispersive X-ray (EDX) mapping revealed a scattered distribution of aluminum

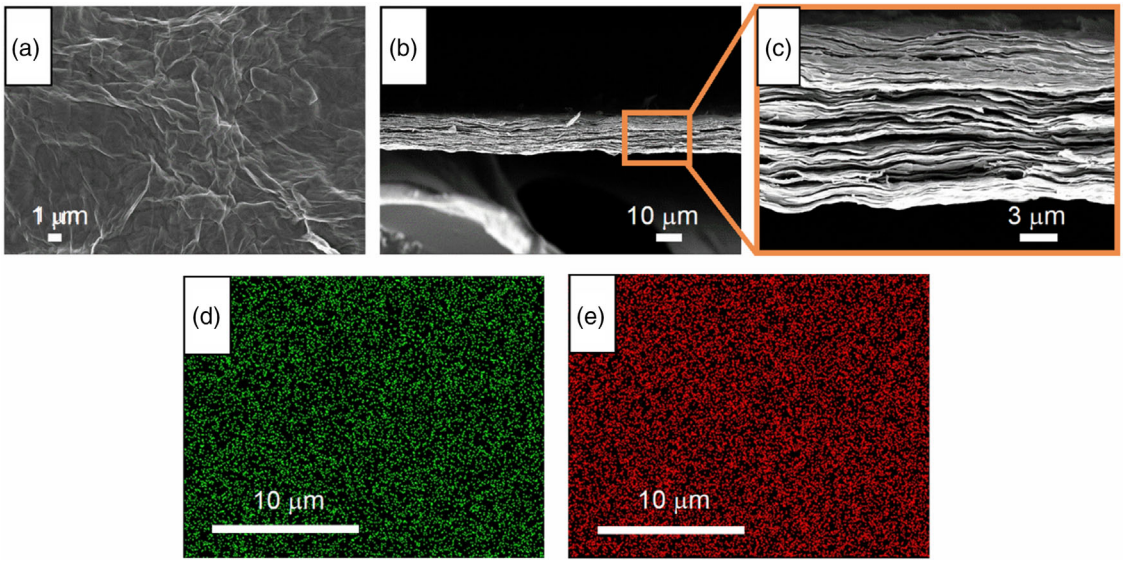

Figure 1. FESEM images of: a) surface of the membranes b,c) a cross-section of the membrane at different magnifications. EDX analyses of the GO–KOH membrane of: d) Al present in the analyzed area, and e) K present in the analyzed area.

(Al) and potassium (K) throughout the examined membrane, as shown in Figure 1d,e, respectively. Even if $Al(OH)_4^-$ remains trapped within the GO membrane, in dry conditions (i.e., the conditions in which X-ray photoelectron spectroscopy (XPS) and EDX analysis are performed), $KAl(OH)_4$ aggregates can also appear in the form of potassium aluminate ($KAlO_2$) or precipitate back into oxides and hydroxides due to a shift in the equilibrium.[40] Consequently, the presence of potassium in the EDX results can be attributed to K^+ cations from both KOH and $KAl(OH)_4$ that interact with the negative oxygen moieties of the GO and $Al(OH)_4^-$ anions and $KAlO_2$. The presence of aluminum can originate either from the trapped $Al(OH)_4^-$ anions, $KAlO_2$, Al_2O_3, or $Al(OH)_3$ precipitates.

The chemical composition of the membrane was investigated via XPS measurements. A survey scan was initially performed to assess the chemical elements present in the membrane and confirmed the presence of both K-based and Al-based compounds in the GO matrix (see Figure S2, Supporting Information). The C 1*s* HR spectrum (**Figure 2**a) was deconvoluted into the usual components that can be found in GO samples,[41] with the C sp^2 peak at 284.5 eV as calibration peak. The reduction degree of GO was found equal to 0.658 and computed from the ratio between the oxidized bonds and the graphitic ones, following Equation (2):

$$\left(\frac{\mathrm{C-OH+O=C-OH}}{\mathrm{C}\,sp^2}\right)_{\mathrm{area}} \quad (2)$$

The O 1*s* peak was deconvoluted into two main components (see Figure 2b). The C═O peak located at 530.7 eV also enveloped the K—O and Al—O bonds, while the C–OH peak located at 532.15 eV also contained the contribution of Al–OH bonds.[42–45] The K 2*p* peak (Figure 2c) was deconvoluted into its $2p_{3/2}$ (at 292.69 eV) and $2p_{1/2}$ peaks (at 295.46 eV). From their position and the $\Delta E \approx 2.8$ eV, it was concluded that the potassium ions were indeed bonded with oxygen atoms.[42] Finally, the HR spectrum of Al 2*p* Figure 2d showed the overlap of the $2p_{3/2}$

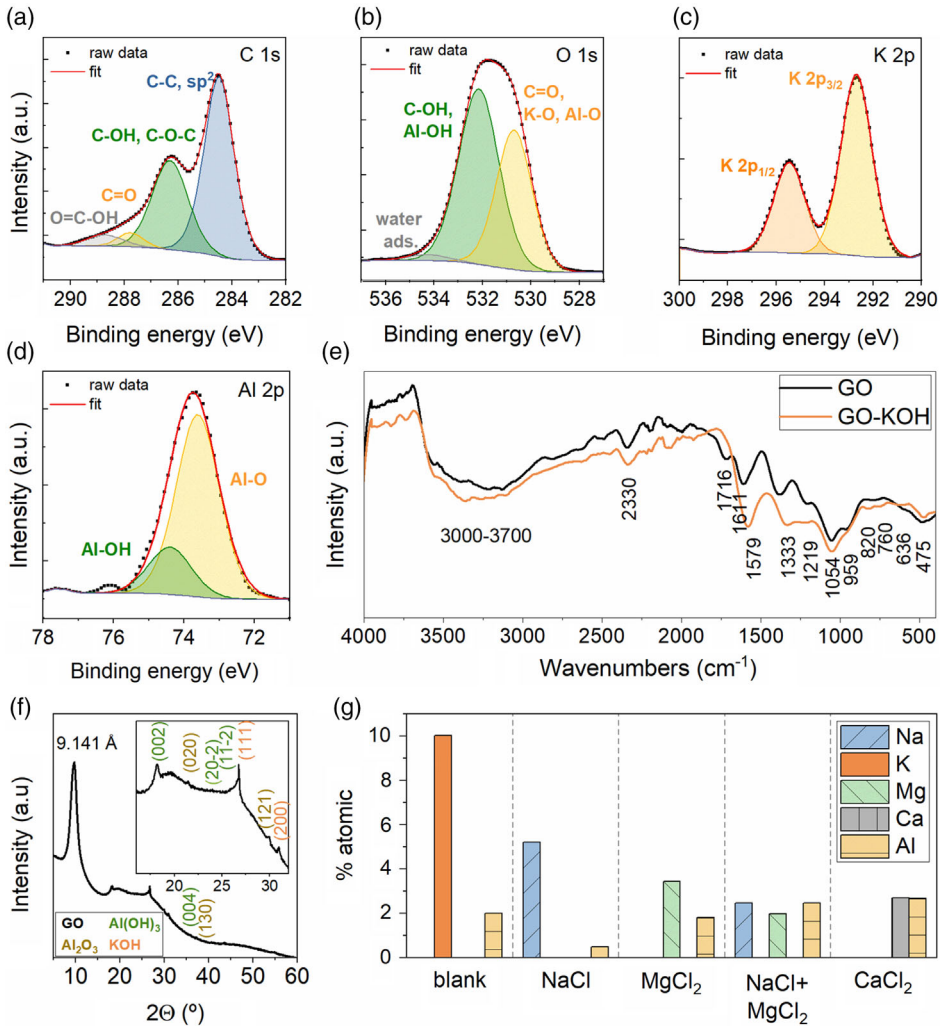

Figure 2. Physico-chemical characterizations of the pristine membrane. XPS HR spectra of a) C 1s, b) O 1s, c) K 2*p*, and d) Al 2*p* components. e) IR spectrum of the GO and GO–KOH membranes, f) XRD diffractogram of the GO–KOH membrane, g) EDX measurements on the blank membrane and the ones tested in NaCl, $MgCl_2$, NaCl + $MgCl_2$, and $CaCl_2$. Blank corresponds to the membrane before doing the electrochemical characterization and the salts are the electrolytes tested for the ionic conductivity measurements.

and $2p_{1/2}$. Nevertheless, the Al peak could be deconvoluted into two contributions. The one at lower binding energies (73.6 eV) could be ascribed to Al—O bonds, while the one at higher energies (74.7 eV) to Al—OH bonds.[40,43,46] Although the content of aluminum atoms in the samples was reasonably low (around 1.3 at%, see Table S1, Supporting Information) the presence of both oxide and hydroxide bonds is compatible with the presence of the anions generated by the alkaline environment of the vacuum filtration process and trapped between GO layers during filtration.

Fourier transform infrared (FTIR) spectroscopy analysis was pursued on pristine GO membranes and after the pretreatment (Figure 2e).[22,47–49] The absorption band between 3000–3700 cm^{-1} corresponds to the stretch vibration of the O—H bonds. The peak at 2330 cm^{-1} is due to the CO_2 present in the environment. Stretch vibrations of the carboxyl groups correspond to the peak at 1716 cm^{-1}. The peaks at 1611 and 1579 cm^{-1} are associated with the C = C groups of the aromatic ring of GO and GO–KOH membranes, respectively. Hydroxyl groups are related to the peaks at 1333 and 1219 cm^{-1}. Stretch vibrations of alkoxy groups (C–O) are associated with the adsorption band at 1054 cm^{-1}.[37] The peak at 959 cm^{-1} corresponds to the epoxy groups of the material. Instead, the peaks at 820 and 475 cm^{-1} correspond to the bending vibrations of Al–O.[50–52] The peaks at 760 and 636 cm^{-1} are associated with the twisting and stretching vibration of Al–O, respectively.[50]

X-ray diffractometry was carried out in the composite sample after drying to identify the interlayer stacking distance and its overall crystallinity. As depicted in Figure 2f, the reflections are quite broad, suggesting amorphicity or short-range order in the carbonaceous sample. A strong peak centered at 9.684° can be ascribed to the stacking distance among the GO layers (9.141 Å in comparison to 8.17 Å for pristine GO) and the very little and sharp peaks superimposed on the broad reflections have been qualitatively assigned to KOH (light-blue), Al_2O_3 (orange), and $Al(OH)_3$ (red) according to COD cards (Figure 2f).

A quantitative analysis of the Na, K, Mg, Ca, and Al elements from the EDX measurement is plotted in Figure 2g. C and O have been excluded from the figure to facilitate its interpretation. The blank corresponds to the GO–KOH membrane obtained after fabrication. The other results correspond to the GO–KOH membranes after the permselectivity measurements in different salts: NaCl, $MgCl_2$, NaCl + $MgCl_2$, and $CaCl_2$. In general, K from the blank is attributed to K^+ cations from KOH and $KAl(OH)_4^-$ trapped within the matrix after the pretreatment which disappear after the selectivity measurements as they redissolve into the electrolyte. Instead, cations from the electrolyte salts remain trapped in the structure after the measurement, due to the exposure of the membrane to a high-concentrated solution during the testing. Nevertheless, the Al quantity remains stable after the measurements, meaning that $Al(OH)_4^-$ anions remain trapped within the GO layers.

To investigate the modification at both surface and bulk levels, EDX measurements were conducted on both the top and the bottom of the pristine membranes. These provide more insights on the depth of the functionalization, given that only one side of the membrane is in contact with the support during the fabrication process. Indeed, as can be seen in **Table 1**, there is a significant difference in the Al amount between the top and the bottom, since only the bottom was in contact with the Al_2O_3 support membrane, but this doesn't affect the membrane performance (see Figure S3, Supporting Information).

Table 1. EDX results on the analysis of the top and bottom side of the GO membrane.

	Atomic [%]	
	Top	Bottom
C	45.3	40.14
O	42.95	46.88
Al	0.34	2.5
S	0.48	NA
K	10	9.63
Pt	0.94	0.84

2.2. Electrochemical Characterization

GO membranes present charge selectivity due to their negatively charged functional groups (hydroxyl, carboxyl, and epoxy).[22,29] This intrinsic surface charge electrostatically repels anions, while allowing the passage of cations. Ion sieving is also achieved by size exclusion, controlled by the interlayer distance between the flakes, also playing a key role in the ion sieving.[22]

The suitability of the membranes to be used as ion exchange membranes was thus evaluated after being immersed for 1 h in the solution to wet it thoroughly and ensure its stability. This timeframe was previously proved to allow the GO membranes to reach a steady state.[22] The permselectivity of the membranes was first studied, as it gives information about the ability of the membranes to repeal the co-ions (i.e., anions). The open-circuit voltage (OCP) that arises at the membrane when exposed to a concentration gradient is compared to the Nernst potential to calculate the permselectivity. The permselectivity of the membranes was measured in KCl solution since the ionic mobilities of K^+ and Cl^- are similar. **Figure 3**b proves the stability of the membranes during the measurement in which the OCP stays stable even when the membrane gets wet. Different concentration gradients were studied to see the combined effect of the electrolyte solution and the salinity gradient on the performances of the membranes. 5, 10, and 100 folds were tested corresponding respectively to 0.1–0.5, 0.1–1, and 0.01–1 M, in an experimental setup like the one in Figure 3a. A potentiostatic linear sweep voltammetry (LSV) (see a measurement example in Figure 3c) was performed to obtain the OCP needed for the permselectivity calculation, which corresponds to the potential when the current is 0 A. While the potential increased linearly with the concentration gradient (Figure 3d), given the increase of the Nernst potential, the permselectivity decreased. This loss in the membranes permselectivity is related to a higher osmotic pressure and a higher swelling of the membranes in diluted solutions (Figure 3e).[22]

GO–KOH membranes presented higher permselectivity than pristine GO membranes due to different reasons: 1) GO reduction and 2) $Al(OH)_4^-$ anions incorporation. GO reduction. It has been previously reported that the reduction of GO

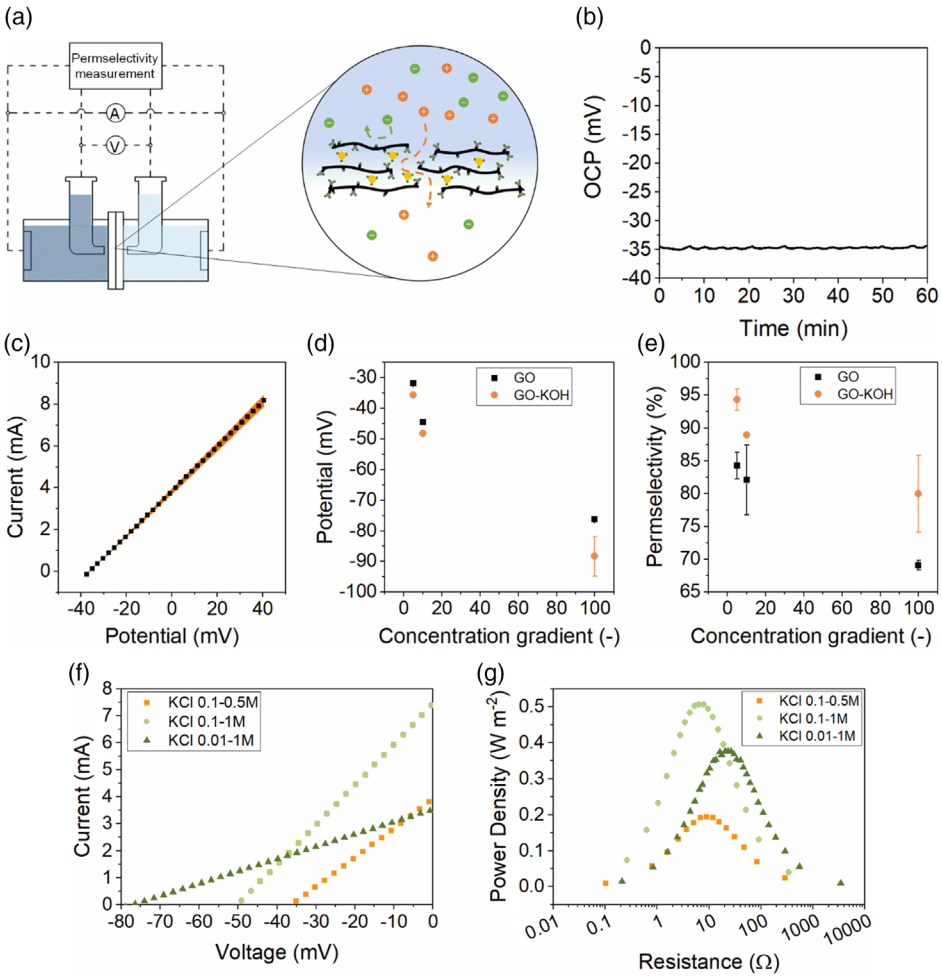

Figure 3. a) Schematic representation of the permselectivity measurement setup. The concentrated solution is represented in a darker shade with respect to the diluted one. b) OCP measurement of the membrane over a 1 h timeframe to ensure its stability. c) Example of the LSV measurement of the GO–KOH membrane in KCl 0.1–0.5 M applying a potential range from −40 to 40 mV. d) Open-circuit potentials of GO (in black) and GO–KOH (in orange) membranes obtained in KCl 0.1–0.5, 0.1–1, and 0.01–1 M. e) Permselectivity of GO (in black) and GO–KOH (in orange) membranes in KCl 0.1–0.5, 0.1–1, and 0.01–1 M f) LSV measurements of GO–KOH membranes in KCl 0.1–0.5, 0.1–1, and 0.01–1 M. g) Power densities obtained for GO–KOH membrane from the LSV measurements under KCl 0.1–0.5, 0.1–1, and 0.01–1 M concentration gradients.

membranes increases their permselectivity due to the shrinking of the channels dimension, and a reduction of the swelling degree.[22] $Al(OH)_4^-$ anions incorporation. The $Al(OH)_4^-$ anions formed during the membrane preparation are incorporated inside the GO matrix increasing the effective negative charge of the membrane channels. As explained in more detail in the modeling (Section 2.3), these anions improve the rejection of the electrolyte anions and enhance the general negative charge of the membrane, therefore increasing its permselectivity.

From the linear sweep potentiostatic measurements at different concentration gradients (Figure 3f) the obtained power density of GO–KOH membranes was measured (Figure 3g) with Ohm's law, obtaining a maximum power density of 0.51 W m^{-2} at 10 folds (i.e., using KCl 0.1-1 M). Power densities increase when moving from 0.1–0.5 to 0.1–1 M because the Nernst potential increases with the salinity gradient. Nevertheless, in the case of KCl 0.01–1 M even if the Nernst potential increases, a simultaneous rise in the resistance of the electrolyte strongly affects the power density that can be generated.

The ionic resistance of ion-exchange membranes is another key parameter when evaluating their performance. The resistance of GO and GO–KOH membranes was analyzed using electrochemical impedance spectroscopy (EIS, **Figure 4**a), LSV (Figure 4b), and chronoamperometry (Figure 4c). measurements, with the same solution on both sides of the membrane as can be seen in Figure 4e. While EIS provides information about the membrane properties in the absence of polarization effects, thus focusing on the materials themselves, chronoamperometry closely approximates the membrane performance in a real stack of membranes. Membrane polarization is the reason for which the resistance increases when testing the membranes with LSV and chronoamperometry with respect to EIS. This happens because EIS applies an oscillating potential that avoids membrane polarization, while LSV applies direct current for

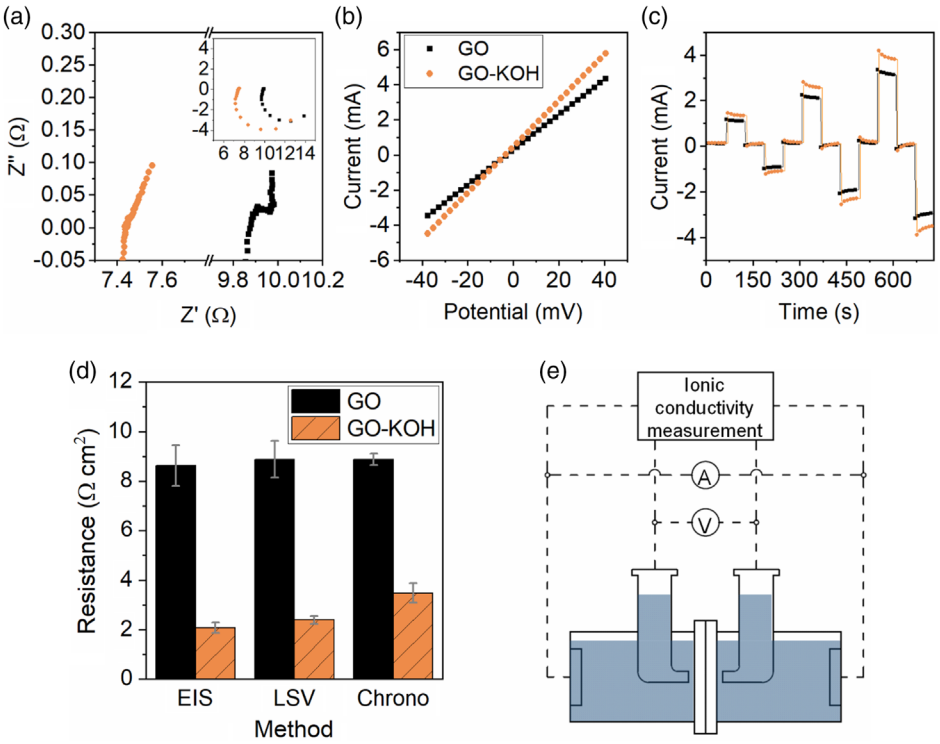

Figure 4. Areal resistance of GO (in black) and GO–KOH (in orange) membranes in NaCl 0.5 M after 1 h: a) EIS, b) LSV, and c) chronoamperometry measurements. d) Comparison of the areal resistances obtained for GO (in black) and GO–KOH (in orange) membranes for each technique. e) Schematic representation of the setup used to measure the ionic resistance.

shorter durations compared to chronoamperometry, in which each step lasts for 60 s.

Notably, GO membranes alone exhibit higher resistances, and the polarization effect is less pronounced compared to GO–KOH membranes (Figure 4d). Specifically, resistances increase from EIS to chronoamperometry by 2.9% for GO membranes, whereas for GO–KOH membranes, the increase is substantially higher at 67.5%. The reduction in the ionic resistance of the GO–KOH membranes is explained by their faster cation transport. This is an effect of the enhanced negative charge induced by the anchoring of $Al(OH)_4^-$ ions in the GO matrix, as detailed in Section 2.3.

Ion exchange selectivity toward mono-valent ions is a property of great interest to improve the generated power densities. This selectivity is calculated as the ratio between the resistances of the membranes toward different ions, given that it evaluates the cation transport of the membrane. The resistances of the membranes were, again, evaluated by means of EIS (**Figure 5**a), LSV (Figure 5b), and chronoamperometry (Figure 5c) to see the polarization effect of the membranes for each cation. GO–KOH membranes exhibited remarkable selectivity toward mono-valent cations, as evidenced by a significant increase in resistance when exposed to divalent cations (Figure 5a–c). Apart from charge selectivity, these GO membranes also demonstrate size selectivity, attributed to the nanometer-sized nanochannels formed between the flakes.

The size of the hydrated radius and the charge of the ions have a clear impact on the ionic resistance of the membranes, as shown in **Figure 6**a. Divalent cations, which are typically more strongly hydrated due to their higher charge and larger size, face increased difficulty in passing through these narrow channels. As a result, the behavior of GO–KOH membranes changes from resistive to significantly capacitive. This increased capacity is due to the high interaction of divalent ions combined with size exclusion, resulting in a lower passage of ions and thus enhanced charge accumulation. The GO–KOH membrane selectivity was compared to a previous study in which the selectivity of different membranes was studied. T. Rijnaarts et al. studied the selectivity of different types of cation exchange membranes: 1) standard-grade: Ralex CMH-PES and Fuji Type I, 2) multivalent-permeable: Fuji T1, and 3) Monovalent-selective: Neosepta CMS. As shown in Figure 6b, the GO–KOH membrane shows a behavior similar to Neosepta CMS membrane, confirming its monovalent-selectivity.

The GO–KOH membranes performance was compared to the one of commercial membranes in terms of permselectivity and ionic resistance.[53–64] As shown in Figure 6c, their performance is in line with the current best-performing membranes commercially available, which holds great promise for their use as a cation-exchange membrane alternative.

2.3. Modeling

To understand the effect of aluminum in GO membranes, atomistic simulations were carried out. When aluminum oxide is dissolved in water, it forms $Al(OH)_4^-$ ions that can interact with the membrane. To determine the way aluminum behaves, two sheets of GO were positioned next to each other to simulate a

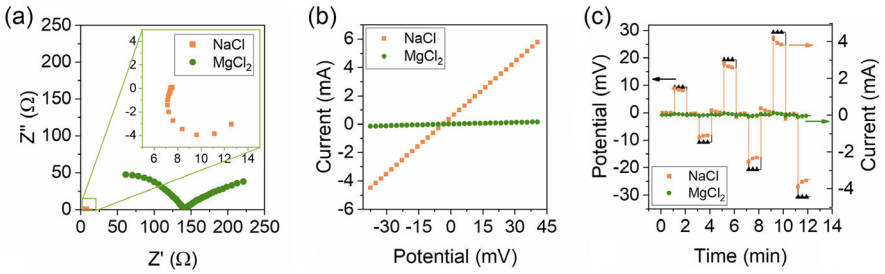

Figure 5. Ionic resistance measurements of GO–KOH after being immersed for 1 h in NaCl (in orange) and $MgCl_2$ (in green) 0.5 M a) EIS b) LSV, and c) chronoamperometry, with the applied potential (in black) and the measured current for NaCl (in orange) and $MgCl_2$ (in green).

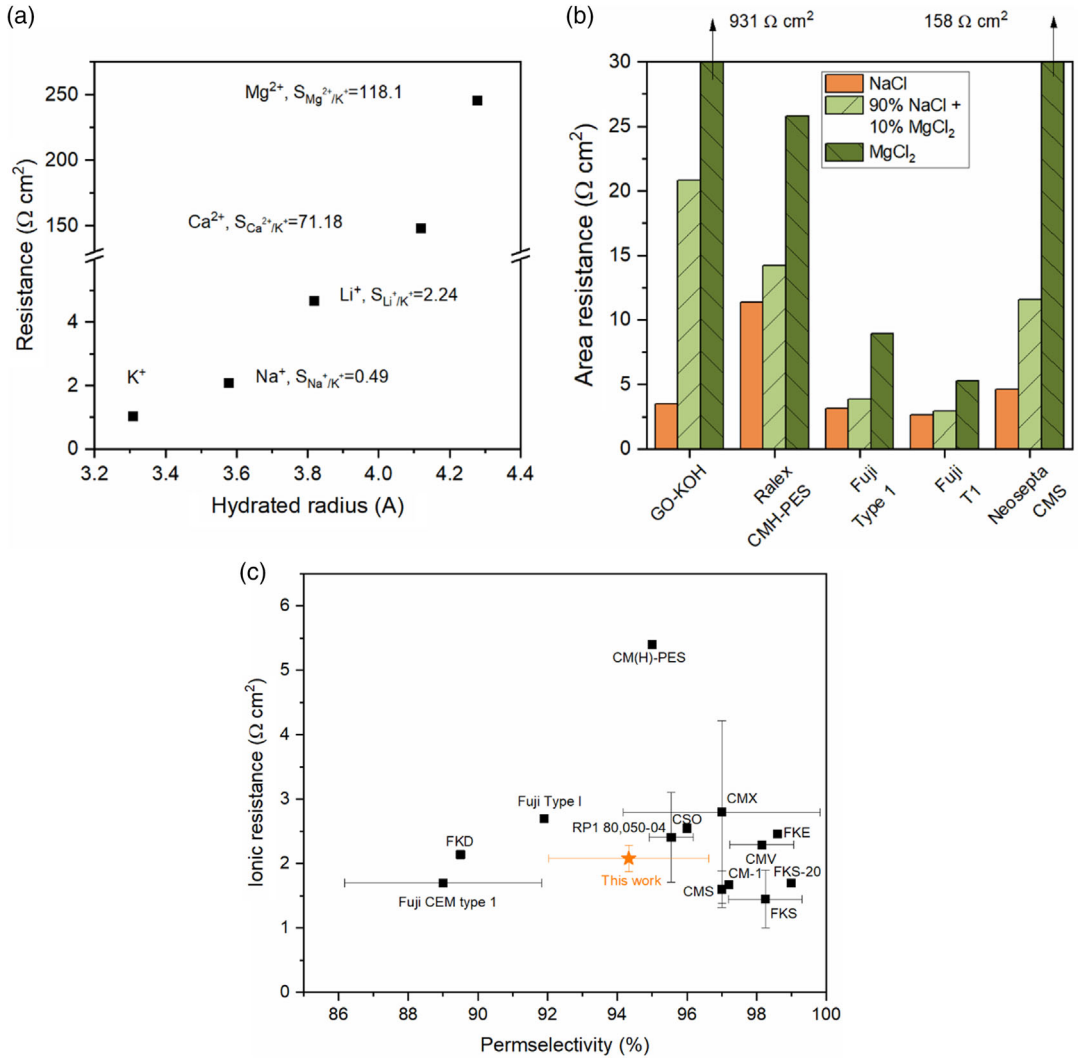

Figure 6. a) Resistance and selectivity of GO–KOH, measured by EIS with different salts after 1 h of immersion. b) Areal resistance of GO–KOH (determined by chronoamperometry) of CEMs in NaCl 0.5 M (in orange), a mixture of 90% NaCl and 10% $MgCl_2$ (in light green) and $MgCl_2$ 0.5 M (dark green), commercial membrane results are from Timon Rijnaarts et al.[68] c) Comparison of Ionic Resistance and Permselectivity of the membrane studied in this work and commercial ones.

bilayer membrane. The space between the two sheets was filled with water molecules and $Al(OH)_4^-$ ions. Interestingly, during dynamics, the Al-containing anion is found to bridge the two GO sheets, as shown in **Figure 7**a. The aluminum ion sits in between the layers while the OH^- groups point their hydrogen atoms toward the GO surfaces. In particular, the hydrogen atoms are found to sit in the middle of an aromatic ring, as seen from the top view of Figure 7a. This behavior is reminiscent of the way

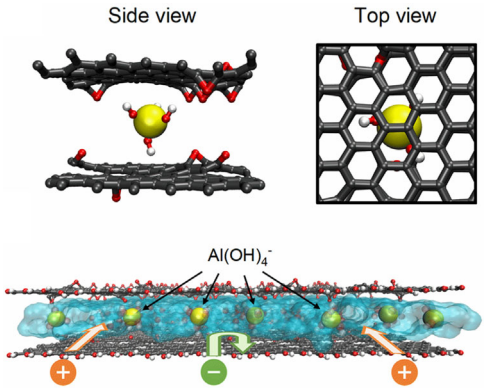

Figure 7. a) Geometry of the bound $Al(OH)_4^-$ ion within the membrane. The C, Al, O, H atoms are depicted respectively in grey, yellow, red, and white. b) Schematic representation of the mechanism of filtration aided by the $Al(OH)_4^-$ ions.

positively charged ions adhere to aromatic compounds by means of cation–π interactions.[65] The relatively large size of $Al(OH)_4^-$ fits the GO interlayer distance, and the OH^- groups, which interact with the carbon atoms of the GO layers, induce a strengthening of the adhesion between GO neighboring sheets. As a result of the aforementioned interaction, $Al(OH)_4^-$ diffusion is particularly slow, $6.3{\cdot}10^{-9}$ $cm^2\,s^{-1}$, because it is mainly dominated by the oscillations of the ion around its bound position. The anchoring effect is observed only when $Al(OH)_4^-$ is confined between two GO sheets. When a single sheet is immersed in water, $Al(OH)_4^-$ is found either to bind to the GO layer in a configuration similar to the one discussed earlier (see the first peak of the atom densities as function of the distance from the GO reported in Figure S4, Supporting Information) or to interact with the oxygen groups of the GO layer at larger distances (see second peak of the atom densities as function of the distance from the GO reported in Figure S4, Supporting Information). The peak corresponding to the first configuration appears to be less intense. However, because the membrane is experimentally produced by vacuum filtration while the aluminum oxide support is dissolving in the water under the effect of KOH, the compression on the GO flakes induced by the process leads to the trapping of $Al(OH)_4^-$ inside the membrane. The small resulting interlayer distance allows for $Al(OH)_4^-$ to interact with the membrane only in the configuration closest to the GO layer. Consequently, it is the confinement between the membrane sheets that promotes this peculiar $Al(OH)_4^-$ arrangement, which stabilizes the bridging configuration and limits the anion diffusion.

By comparison, a monovalent anion like Cl^- shows a completely different behavior when confined within GO. Chloride does not bind to the surface, but rather it hovers at an average distance of 4.1 Å from the GO layer in the mid part of the channel as illustrated in SI. Consequently, the Cl^- diffusivity is much higher than $Al(OH)_4^-$, 2.2×10^{-7} $cm^2\,s^{-1}$, so chlorine, when fluxed in, does not get blocked in the GO but is likely, once entered in the membrane, to permeate through.

Based on these results, we can rationalize the reasons behind the improved performance of the GO–KOH membrane over the regular GO membranes. The KOH produces dissolved $Al(OH)_4^-$ in water. Once the $Al(OH)_4^-$ anions enter the membrane, they bind to the membrane bridging two facing layers. An accumulation of negative charges within the membrane and, in particular, at the membrane entrance is created, as schematically illustrated in Figure 7b. The salt cations' access to the membrane is then favored by $Al(OH)_4^-$, while anions are electrostatically repelled leading to an overall improvement in terms of performance. So, even if the GO surface negative charge decreases as a result of the KOH reduction process, thanks to the presence of $Al(OH)_4^-$ ions the overall effectiveness in transporting cations is improved. The mechanism is similar to the one that enhances selectivity in functionalized nanoporous graphene membranes, where the electrostatic interaction between membrane and filtered particles improves the permeance of polarized or charged species.[66]

3. Conclusion

GO membranes hold great promise as alternatives to conventional polymeric membranes. Nevertheless, they still present challenges related to high ionic resistance. To address this issue, this study proposes a novel approach incorporating $Al(OH)_4^-$ anions into the GO matrix. This unique integration of anions enhances ion diffusion and selectivity, due to an increased general negative charge density, as supported by the modeling results.

A permselectivity of nearly 95% and an ionic resistance of only 2 Ω cm^2 were achieved, representing a substantial improvement over previous works in literature. Additionally, the membranes exhibited outstanding mono-valent selectivity, a crucial factor for enhancing the power density of RED processes.

In conclusion, the successful incorporation of $Al(OH)_4^-$ anions into the GO matrix represents an exciting advancement in membrane technology, overcoming the challenges associated with high ionic resistance and offering great potential for various practical applications. These results highlight how this approach surpasses existing membrane technologies based on graphene, paving the way toward its use as a possible replacement for polymeric membranes which have a high cost and environmental impact.

4. Experimental Section

Materials: Graphene oxide (2.5 wt% dispersion) was purchased from Graphenea. All chemicals were supplied by Merck. The chemicals used were lithium chloride (LiCl, ≥99%), sodium chloride (NaCl, ≥99%), potassium chloride (KCl, ≥99%), calcium chloride ($CaCl_2$, ≥99%), magnesium chloride ($MgCl_2$, ≥98%), potassium hydroxide (KOH, 85%). Anodisc supports with a pore size of 0.2 µm were acquired from Whatman. Activated carbon provided by Kuraray, carbon black C65 provided by Imerys, and PTFE (form 60% water suspension provided by Sigma Aldrich) were used for the working and counter electrodes preparation.

Membrane Fabrication: A dispersion of GO and KOH with a weight ratio GO:KOH of 1:1.5 was prepared and stirred overnight, achieving a final GO concentration of 5 mg mL^{-1}. Membranes were fabricated by using vacuum filtration. Briefly, 5 mL of the GO dispersion (with and without KOH) were filtrated through an Anodisc support. After the filtration, the membrane was detached from the support by heating it up to 80 °C on a heating plate.

Membrane Characterization: Field-emission scanning electron microscopy (FESEM Supra 40, manufactured by Zeiss) equipped with an Oxford Si(Li) detector for EDX was used to investigate the morphology of the membranes. The cross-section of the membrane was examined to confirm the homogeneity and order degree of the flakes inside the matrix.

GO membranes were analyzed by FTIR spectroscopy (Nicolet 5700 FTIR, Thermo Fisher Scientific), and X-ray diffraction (XRD, X'Pert pro, Malvern Panalytical). For the FTIR analysis, all the membranes were kept under vacuum for 24 h to avoid the contribution from atmospheric moisture.

The chemical composition was investigated through XPS by using a PHI 5000 VersaProbe system (Physical Electronics, Inc. (PHI), Chanhassen, MN, USA). Monochromatic Al Kα (1486.6 eV) was used as X-ray source, and the C–C sp^2 peak in graphitic structures (284.5 eV) was used as reference for the calibration. Wide-energy and high-resolution (HR) XPS spectra were collected and processed using CasaXPS software (version 2.3.18). HR spectra deconvolution into individual mixed Gaussian–Lorentzian peaks was obtained after Shirley background subtraction and binding energy (BE) calibration.

Diffraction patterns of the sample were collected on a powder X-ray diffractometer (Empyrean, Anton Paar, STATE) with Cu Kα radiation ($\lambda = 1.54052$ Å) at 40 kV, and 30 mA, and a 0.013 step size of 2θ angle from 5° to 60°. The samples were placed onto a zero-background stage holder to avoid further signals. The software QualX with RRUFF- and COD-database was used for the phase identifications. The COD cards are 1 000 061, 1 000 442, 9 008 655. Interlayer distances between flakes of GO membranes were evaluated using the Bragg law.

Electrochemical Measurements: Permselectivity and ionic resistance were measured in a side-by-side cell. Ag/AgCl reference electrodes were placed as close to the membrane as possible using Luggin's capillaries. Each capillary was filled with the corresponding electrolyte solution used in the half-cell. Carbon-based electrodes were used as working and counter electrodes. 85% of activated carbon, 10% of carbon black C65, 5% of PTFE (form 60% water suspension) were mixed in excess ethanol at 60 °C. The solution was let dry while stirring until the formation of a wet dough, which was calendered several times to get a self-standing carbon layer. The electrodes were cut and dried at 60 °C overnight. Afterwards, they were placed in a titanium mesh folded to grip the carbon material. The membrane with an active area of 1.77 cm^2 was placed between each half-cell and pressed with two polydimethylsiloxane o-rings. Finally, electrolyte solutions were flowed at a rate of 5 mL min^{-1} during the whole experiment to keep the concentration fixed inside the cell and avoid membrane polarization. All measurements were run by a potentiostat (PGSTAT302N) equipped with a frequency response analyzer that was controlled by NOVA 2.1 software (Metrohm Autolab, The Netherlands).

Permselectivity was measured in KCl under different concentration gradients (0.01–1, 0.1–1, and 0.1–0.5 M). Permselectivity is measured as stated in Equation (3),[22,67] where E_{mem} corresponds to the open-circuit potential measured without the contribution of the potential difference between the two Ag/AgCl reference electrodes (ΔE_{offset}), and the junction potential (ΔE_j) as shown in Equation (4).[22,67] E_{meas} is obtained from a potentiostatic linear sweep voltammetry (LSV) measurement from $-40\ mV_{OCP}$ to $+40\ mV_{OCP}$. Instead, E_{the} corresponds to the Nernst potential calculated as in Equation (5), in which R is the gas constant, T is the temperature, z is the valence of the ion, F is the Faraday constant and a corresponds to the activity of the species. Finally, permselectivity also considers the transport number of the counter-ions (t_g) and co-ions (t_c) as stated in Equation (3).[22,67]

$$\alpha_{tn} = \frac{\frac{E_{mem}}{E_{the}} + 1 - 2t_g}{2t_c} \tag{3}$$

$$E_{mem} = E_{meas} - \Delta E_{offset} - \Delta E_j \tag{4}$$

$$E_{the} = -\frac{RT}{zF} \ln\left(\frac{a_i}{a_j}\right) \tag{5}$$

The ionic conductivity was measured in LiCl 0.5 M, NaCl 0.5 M, KCl 0.5 M, $MgCl_2$ 0.5 M, and $CaCl_2$ 0.5 M. Also, a mix of NaCl 0.45 M and $MgCl_2$ 0.05 M was tested to see the influence of mono and bivalent ions together. The setup is the same as the one used to measure the permselectivity.[22] Nevertheless, in this case, the same electrolyte at the same concentration was placed on each side of the membrane. Three electrochemical measurements were done: 1) Electrochemical impedance spectroscopy (EIS), 2) potentiostatic LSV, and 3) Chronoamperometry.

EIS: a frequency range from 10^5 to 0.1 Hz with an amplitude of 5 mV was applied. The resistance corresponds to the real part of the impedance when the imaginary part is 0 Ω.

Potentiostatic LSV: as for the permselectivity, a potential range from $-40\ mV_{OCP}$ to $+40\ mV_{OCP}$ was applied. The resistance corresponds to the inverse of the slope of the obtained results.

Chronoamperometry: a fixed potential of 0, ±10, ±20, and ±30 mV was applied for 60 s while measuring the current. The last ten seconds of each applied potential were averaged and current versus potential was plotted. As for the LSV, the resistance corresponds to the inverse of the slope of the obtained data. The obtained resistances (R_{meas}) correspond to the sum of the resistance of the membrane (R_m), and the one of the electrolytes between the Luggin's capillaries (R_{blank}) (Equation (6)). Blanks were measured using the same set-up configuration without placing the membrane. R_m was multiplied by the exposed area of the membrane, 1.77 cm^2.

$$R_m = R_{meas} - R_{blank} \tag{6}$$

The selectivity of the membrane toward cations of different size and charge was evaluated according to the membrane resistance in each electrolyte. The transport selectivity corresponds to the ratio of these resistances as in Equation (7).[68] The resistance obtained in NaCl was taken as reference.

$$S_{Mg}^{Na} = \frac{R_{Mg}}{R_{Na}} \tag{7}$$

Modeling: Classical molecular dynamics simulations were performed by means of the LAMMPS software package.[69,70]

As first step, a realistic structure of a GO flake was obtained by means of REAXFF potential,[71] already widely employed to describe the structure of GO flakes for filtration.[72–74] Oxygen single atoms were distributed on the surface of a 129 × 128 $Å^2$ graphene flake and allowed to chemically bond with the sheet, as previously done in the literature.[74] The edges of the sheet were saturated with hydroxyl groups. The reactions occurred at the controlled temperature of 300 K maintained by a Nosé–Hoover thermostat for a time of 200 ps to allow for possible diffusion or desorption of the ions. The final coverage was 10%. The resulting structure was then employed in subsequent GO membrane simulations.

To simulate the behavior of the ion containing solution within the GO membrane, two facing GO sheets were positioned in a supercell. The space between the GO sheets was filled with 2625 molecules of water, 25 K^+ ions, and either 25 $Al(OH)_4^-$ or Cl^-. The atomic positions of GO were fixed. Only one of the two layers was allowed to move rigidly in the direction perpendicular to the layer under the effect of pressure, to correctly describe the membrane's structure. The final interlayer distance, ≈9 Å, resulted in being consistent with the experiments. A vacuum layer of more than 180 Å was placed to avoid replica interactions in the direction of the applied pressure. In all other directions, periodic boundary conditions were applied. The calculation was run for 8 ns with a timestep of 1 fs. An additional test involved a single GO layer surrounded by 3400 water molecules, 50 $Al(OH)_4^-$, and 50 K^+. Similarly to what is reported earlier, the calculation was run for 8 ns. For the simulations with water, the force field of the membrane was changed from REAX-FF to a combination of Lennard-Jones and Coulombic forces resulting from point charges assigned to each atom. Lennard-Jones parameters were taken from the literature.[65,75] Local charges on the sheet were calculated by means of Hartree–Fock calculations and the RESP algorithm,[76] as previously done in the literature.[77] For the dissolved ions, Lennard-Jones parameters and

charges were taken from literature for $Al(OH)_4^-$[78] and KCl.[79] Water was described with the TIP4P potential.[80]

Supporting Information

Supporting Information is available from the Wiley Online Library or from the author.

Acknowledgements

This project has received funding from the European Union's Horizon 2020 research and innovation program within the project "intelligent Water Treatment Technologies for water preservation combined with simultaneous energy production and material recovery in energy-intensive industries—intelWATT" (grant agreement no. 958454).

Conflict of Interest

The authors declare no conflict of interest.

Data Availability Statement

The data that support the findings of this study are available from the corresponding author upon reasonable request.

Keywords

2D materials, blue energy, graphene, ion separation, ion-exchange membranes

Received: March 18, 2024
Revised: April 24, 2024
Published online:

[1] UN DESA. The Sustainable Development Goals Report, UN DESA, New York, USA **2022** https://unstats.un.org/sdgs/report/2022/ (accessed: July 2022).
[2] UN. Transforming Our World: The 2030 Agenda for Sustainable Development. Resolution Adopted by the General Assembly on September **2015**, 42809, 1–13.
[3] A. T. Jones, W. Finley, in *Oceans 2003. Celebrating the Past ... Teaming Toward the Future (IEEE Cat. No.03CH37492)*, Vol. *4*, IEEE, Piscataway, NJ **2003**, pp. 2284–2287.
[4] S. Chae, H. Kim, J. Gi Hong, J. Jang, M. Higa, M. Pishnamazi, J.-Y. Choi, R. Chandula Walgama, C. Bae, I. S. Kim, J.-S. Park, *Chem. Eng. J.* **2023**, *452*, 139482.
[5] R. E. PATTLE, *Nature* **1954**, *174*, 660.
[6] B. E. Logan, M. Elimelech, *Nature* **2012**, *488*, 313.
[7] G. Z. Ramon, B. J. Feinberg, E. M. V. Hoek, *Energy Environ. Sci.* **2011**, *4*, 4423.
[8] J. G. Hong, W. Zhang, J. Luo, Y. Chen, *Appl. Energy* **2013**, *110*, 244.
[9] D. A. Vermaas, J. Veerman, N. Y. Yip, M. Elimelech, M. Saakes, K. Nijmeijer, *ACS Sustainable Chem. Eng.* **2013**, *1*, 1295.
[10] R. A. Tufa, S. Pawlowski, J. Veerman, K. Bouzek, E. Fontananova, G. di Profio, S. Velizarov, J. Goulão Crespo, K. Nijmeijer, E. Curcio, *Appl. Energy* **2018**, *225*, 290.
[11] A. Nazif, H. Karkhanechi, E. Saljoughi, S. M. Mousavi, H. Matsuyama, *J. Water Process Eng.* **2022**, *47*, 102706.
[12] M. Macha, S. Marion, V. V. R. Nandigana, A. Radenovic, *Nat. Rev. Mater.* **2019**, *4*, 588.
[13] W. Xin, L. Jiang, L. Wen, *Acc. Chem. Res.* **2021**, *54*, 4154.
[14] K. Fan, S. Zhou, L. Xie, S. Jia, L. Zhao, X. Liu, K. Liang, L. Jiang, B. Kong, *Adv. Mater.* **2024**, *36*, 2307849.
[15] L. Xie, S. Zhou, J. Liu, B. Qiu, T. Liu, Q. Liang, X. Zheng, B. Li, J. Zeng, M. Yan, Y. He, X. Zhang, H. Zeng, D. Ma, P. Chen, K. Liang, L. Jiang, Y. Wang, D. Zhao, B. Kong, *J. Am. Chem. Soc.* **2021**, *143*, 6922.
[16] S. Zhou, L. Xie, M. Yan, H. Zeng, X. Zhang, J. Zeng, Q. Liang, T. Liu, P. Chen, L. Jiang, B. Kong, *Analyst* **2022**, *147*, 652.
[17] L. Zhang, S. Zhou, L. Xie, L. Wen, J. Tang, K. Liang, X. Kong, J. Zeng, R. Zhang, J. Liu, B. Qiu, L. Jiang, B. Kong, *Small* **2021**, *17*, 2100141.
[18] J. Ji, Q. Kang, Y. Zhou, Y. Feng, X. Chen, J. Yuan, W. Guo, Y. Wei, L. Jiang, *Adv. Funct. Mater.* **2017**, *27*, 1603623.
[19] Z. Zhang, W. Shen, L. Lin, M. Wang, N. Li, Z. Zheng, F. Liu, L. Cao, *Adv. Sci.* **2020**, *7*, 2000286.
[20] Z. Zhang, S. Yang, P. Zhang, J. Zhang, G. Chen, X. Feng, *Nat. Commun.* **2019**, *10*, 2920.
[21] S. Hong, F. Ming, Y. Shi, R. Li, I. S. Kim, C. Y. Tang, H. N. Alshareef, P. Wang, *ACS Nano* **2019**, *13*, 8917.
[22] A. Aixalà-Perelló, A. Pedico, M. Laurenti, E. Fontananova, S. Bocchini, I. V. Ferrari, A. Lamberti, *NPJ 2D Mater. Appl.* **2023**, *7*, 46.
[23] J. Hao, Q. Sun, W. Wang, M. Zhao, H. Liu, X. Sui, *J. Power Sources* **2023**, *560*, 232701.
[24] J. Gao, X. Liu, Y. Jiang, L. Ding, L. Jiang, W. Guo, *Small* **2019**, *15*, 1804279.
[25] L. Ding, D. Xiao, Z. Zhao, Y. Wei, J. Xue, H. Wang, *Adv. Sci.* **2022**, *9*, 2202869.
[26] Y.-C. Liu, L.-H. Yeh, M.-J. Zheng, K. C.-W. Wu, *Sci. Adv.* **2021**, *7*, eabe9924.
[27] Z. Zhang, L. He, C. Zhu, Y. Qian, L. Wen, L. Jiang, *Nat. Commun.* **2020**, *11*, 875.
[28] Z. Y. Leong, Z. Han, G. Wang, D. S. Li, S. A. Yang, H. Y. Yang, *J. Mater. Chem. A* **2021**, *9*, 244.
[29] A. Pedico, L. Baudino, A. Aixalà-Perelló, A. Lamberti, *Green Methods for the Fabrication of Graphene Oxide Membranes: From Graphite to Membranes*, Membranes **2023**, *13*, p. 429.
[30] R. K. Joshi, P. Carbone, F. C. Wang, V. G. Kravets, Y. Su, I. V. Grigorieva, H. A. Wu, A. K. Geim, R. R. Nair, *Science* **2014**, *343*, 752.
[31] J. Pei, X. Zhang, L. Huang, H. Jiang, X. Hu, *RSC Adv.* **2016**, *6*, 101948.
[32] Y. Li, S. Yuan, Y. Xia, W. Zhao, C. D. Easton, C. Selomulya, X. Zhang, *J. Membr. Sci.* **2020**, *601*, 117900.
[33] J. Hao, Y. Ning, Y. Hou, S. Ma, C. Lin, J. Zhao, C. Li, X. Sui, *J. Colloid Interface Sci.* **2023**, *630*, 795.
[34] K. H. Lee, H. Park, W. Eom, D. J. Kang, S. H. Noh, T. H. Han, *J. Mater. Chem. A* **2019**, *7*, 23727.
[35] S. R. Kwon, J. Harris, T. Zhou, D. Loufakis, J. G. Boyd, J. L. Lutkenhaus, *ACS Nano* **2017**, *11*, 6682.
[36] Y. Wu, W. Xin, X. Y. Kong, J. Chen, Y. Qian, Y. Sun, X. Zhao, W. Chen, L. Jiang, L. Wen, *Mater. Horiz.* **2020**, *7*, 2702.
[37] Y. Qian, D. Liu, G. Yang, L. Wang, Y. Liu, C. Chen, X. Wang, W. Lei, *J. Am. Chem. Soc.* **2022**, *144*, 13764.
[38] Y. Qian, J. Shang, D. Liu, G. Yang, X. Wang, C. Chen, L. Kou, W. Lei, *J. Am. Chem. Soc.* **2021**, *143*, 5080.
[39] C. N. Yeh, K. Raidongia, J. Shao, Q. H. Yang, J. Huang, *Nat. Chem.* **2015**, *7*, 166.
[40] A. P. de Kroon, G. W. Schäfer, F. Aldinger, *J. Alloys Compd.* **2001**, *314*, 147.
[41] D. Yang, A. Velamakanni, G. Bozoklu, S. Park, M. Stroller, R. D. Piner, S. Stankovich, I. Jung, D. A. Field, C. A. Ventrice Jr., R. S. Ruoff, *Carbon N Y* **2009**, *47*, 145.

[42] S. Kim, K. Choi, Y. Shim, S. Lee, S. Park, *Chem. - Eur. J.* **2016**, *22*, 11435.
[43] L. Zhang, Y. Li, H. Guo, H. Zhang, N. Zhang, T. Hayat, Y. Sun, *Environ. Pollut.* **2019**, *248*, 332.
[44] J. S. Lee, H. S. Kim, N. K. Park, T. J. Lee, M. Kang, *Chem. Eng. J.* **2013**, *230*, 351.
[45] J. Zähr, S. Oswald, M. Türpe, H. J. Ullrich, U. Füssel, *Vacuum* **2012**, *86*, 1216.
[46] J. T. Kloprogge, L. V. Duong, B. J. Wood, L. Frost Ray, *J. Colloid Interface Sci.* **2006**, *296*, 572.
[47] Y. M. Shulga, N. Y. Shulga, Y. N. Parkhomenko, *Mod. Electron. Mater.* **2015**, *1*, 1.
[48] Y. Mao, M. Zhang, L. Cheng, J. Yuan, G. Liu, L. Huang, M. Barboiu, W. Jin, *J. Membr. Sci.* **2020**, *595*, 117545.
[49] T. F. Emiru, D. W. Ayele, *Egypt. J. Basic Appl. Sci.* **2017**, *4*, 74.
[50] L. Zhang, Y. Wu, L. Zhang, Y. Wang, M. Li, *Vacuum* **2016**, *133*, 1.
[51] R. Romero Toledo, V. Ruiz Santoyo, D. Moncada Sánchez, M. Martínez Rosales, *Nova Scientia* **2018**, *10*, 83.
[52] T. Kolar, B. Mušič, R. C. Korošec, V. Kokol, *Cellulose* **2021**, *28*, 9441.
[53] P. Długołecki, K. Nymeijer, S. Metz, M. Wessling, *J. Membr. Sci.* **2008**, *319*, 214.
[54] E. Guler, Y. Zhang, M. Saakes, K. Nijmeijer, *ChemSusChem* **2012**, *5*, 2262.
[55] S. Mehdizadeh, M. Yasukawa, T. Abo, M. Kuno, Y. Noguchi, M. Higa, *Membranes* **2019**, *9*, 73.
[56] S. Mehdizadeh, M. Yasukawa, T. Abo, Y. Kakihana, M. Higa, *J. Membr. Sci.* **2019**, *572*, 271.
[57] J. Moreno, V. Díez, M. Saakes, K. Nijmeijer, *J. Membr. Sci.* **2018**, *550*, 155.
[58] J. Moreno, N. de Hart, M. Saakes, K. Nijmeijer, *Water Res.* **2017**, *125*, 23.
[59] G. M. Geise, H. J. Cassady, D. R. Paul, B. E. Logan, M. A. Hickner, *Phys. Chem. Chem. Phys.* **2014**, *16*, 21673.
[60] J. G. Hong, Y. Chen, *J. Membr. Sci.* **2014**, *460*, 139.
[61] M. Tedesco, E. Brauns, A. Cipollina, G. Micale, P. Modica, G. Russo, J. Helsen, *J. Membr. Sci.* **2015**, *492*, 9.
[62] J. G. Hong, T.-W. Park, Y. Dhadake, *J. Electroanal. Chem.* **2019**, *850*, 113437.
[63] H. Zhang, D. Jiang, B. Zhang, J. G. Hong, Y. Chen, *Electrochim. Acta* **2017**, *239*, 65.
[64] M. N. Z. Abidin, M. M. Nasef, J. Veerman, *Desalination* **2022**, *537*, 115854.
[65] E. A. Orabi, G. Lamoureux, *J. Chem. Theory Comput.* **2012**, *8*, 182.
[66] G. Tronci, F. Raffone, G. Cicero, *Appl. Sci.* **2018**, *8*, 1547.
[67] R. S. Kingsbury, S. Flotron, S. Zhu, D. F. Call, O. Coronell, *Environ. Sci. Technol.* **2018**, *52*, 4929.
[68] T. Rijnaarts, E. Huerta, W. Van Baak, K. Nijmeijer, *Environ. Sci. Technol.* **2017**, *51*, 13028.
[69] S. Plimpton, *J. Comput. Phys.* **1995**, *117*, 1.
[70] A. P. Thompson, H. M. Aktulga, R. Berger, D. S. Bolintineanu, W. M. Brown, P. S. Crozier, P. J. in 't Veld, A. Kohlmeyer, S. G. Moore, T. D. Nguyen, R. Shan, M. J. Stevens, J. Tranchida, C. Trott, S. J. Plimpton, *Comput. Phys. Commun.* **2022**, *271*, 108171.
[71] K. Chenoweth, A. C. T. Van Duin, W. A. Goddard, *J. Phys. Chem. A* **2008**, *112*, 1040.
[72] L. C. Lin, J. C. Grossman, *Nat. Commun.* **2015**, *6*, 8335.
[73] F. Raffone, F. Savazzi, G. Cicero, *J. Phys. Chem. Lett.* **2019**, *10*, 7492.
[74] F. Raffone, F. Savazzi, G. Cicero, *Phys. Chem. Chem. Phys.* **2021**, *23*, 11831.
[75] J. Wang, R. M. Wolf, J. W. Caldwell, P. A. Kollman, D. A. Case, *J. Comput. Chem.* **2004**, *25*, 1157.
[76] C. I. Bayly, P. Cieplak, W. D. Cornell, P. A. Kollman, *J. Phys. Chem.* **1993**, *97*, 10269.
[77] F. Raffone, A. Lamberti, G. Cicero, *Electrochim. Acta* **2023**, *458*, 142344.
[78] T. M. C. Faro, G. P. Thim, M. S. Skaf, *J. Chem. Phys.* **2010**, *132*, 114509.
[79] H. Yu, T. W. Whitfield, E. Harder, G. Lamoureux, I. Vorobyov, V. M. Anisimov, A. D. MacKerell, B. Roux, *J. Chem. Theory Comput.* **2010**, *6*, 774.
[80] W. L. Jorgensen, J. Chandrasekhar, J. D. Madura, R. W. Impey, M. L. Klein, *J. Chem. Phys.* **1983**, *79*, 926.